Research Article

In Situ Investigation of Complex BaSO Fiber Generation in the Presence of Sodium Polyacrylate. 2. Crystallization Mechanisms

Tongxin Wang, Antje Reinecke, and Helmut Clfen

Langmuir, **2006**, 22 (21), 8986-8994• DOI: 10.1021/la060985j • Publication Date (Web): 30 June 2006

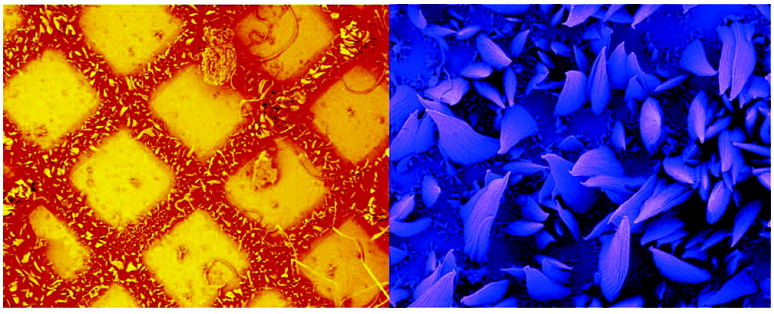

In Situ Investigation of Complex $BaSO_4$ Fiber Generation in the Presence of Sodium Polyacrylate. 2. Crystallization Mechanisms

Tongxin Wang,[†,§] Antje Reinecke,[‡] and Helmut Cölfen*[,†]

Max-Planck Institute of Colloids and Interfaces, Colloid Chemistry Department and Theory Department, Research Campus Golm, Am Mühlenberg, D-14424 Potsdam, Germany

Received April 11, 2006. In Final Form: May 26, 2006

The formation mechanisms of complex $BaSO_4$ fiber bundles and cones in the presence of polyacrylate sodium salt via a bioinspired approach at ambient temperature in an aqueous environment are reported. These complex organic−inorganic hybrid structures assemble after heterogeneous nucleation of amorphous precursor particle aggregates on polar surfaces, and the crystallization area can be patterned. In contrast to earlier reports, three different mechanisms based on the oriented attachment of nanoparticles were revealed for the formation of typical fibrous superstructures depending on the supersaturation or on the number of precursor particles. (A) High supersaturation ($S > 2$): large amorphous aggregates stick to a polar surface, form fiber bundles after mesoscopic transformation and oriented attachment, and then form a narrow tip through polymer interaction. (B) Low supersaturation ($S = 1.02-2$): only a few fibers nucleate heterogeneously from a single nucleation spot, and amorphous particles stick to existing fibers, which results in the formation of a fiber bundle. (C) Vanishing supersaturation ($S = 1-1.02$): nucleation of a fiber bundle from a single nucleation spot with self-limiting repetitive growth as a result of the limited amount of building material. These growth processes are supported by time-resolved optical microscopy in solution, TEM, SEM, and DLS.

Introduction

Biominerals in natural organisms have attracted increasing interest because of their important optical and mechanical properties induced by unique morphologies and arrangements of crystals. For example, the optical properties of pearls and the mechanical properties of teeth and bones have many advantages over those of corresponding synthetic crystals.[1,2] One important feature of biomineralization is the precisely controlled deposition of crystalline material to form organic−inorganic hybrid materials with complex morphology, usually organized over several hierarchical levels.[1]

Consequently, bioinspired syntheses of crystals with complex forms, which mimic natural biominerals, have become a hot research field.[3−12] Improved mechanical material properties of simple inorganic systems, synthesized by a bioinspired approach at ambient temperature in an aqueous environment, are highly attractive to materials chemists. Recent results were reported by Kotov et al. regarding nacre mimicking by a $CaCO_3$ polyelectrolyte multilayer assembly[13] and by Gehrke et al. regarding nacre synthesized in its natural organic matrix.[14] However, in many cases, the formation mechanism of the complex organic−inorganic hybrid materials is unknown, which is an obstacle to obtaining a deeper understanding of the formation of such complex hybrid materials.

One-dimensional crystals are much more interesting because of their altered optical, electrical, and mechanical properties as compared to their three-dimensional counterparts.[15] An interesting $BaSO_4$ and $BaCrO_4$ fiber bundle formed by polymer-directed crystallization in the presence of double hydrophilic block copolymers,[16−21] mixtures thereof,[22] or simple polyacrylate[18,23] was recently reported. These fibers are very similar to $BaSO_4$ fibers formed in reverse microemulsion.[24,25] Different structures, including long bundles or short cones, were obtained. It was suggested that these complex structures form by heterogeneous nucleation on glass surfaces via amorphous precursors, but the formation mechanism was only partially revealed.[18] In fact, many kinds of 1D materials (nanowires and nanochains) were grown with template-directed synthesis,[26−28] vapor-phase synthesis,[29]

* Corresponding author. E-mail: coelfen@mpikg-golm.mpg.de. Tel: ++49-331-567-9513. Fax: ++49-331-567-9502.

† Max-Planck Institute of Colloids and Interfaces, Colloid Chemistry Department.

‡ Max-Planck Institute of Colloids and Interfaces, Theory Department.

§ Present address: Department of Materials Science and Engineering, University of Pennsylvania, 3231 Walnut Street, Philadelphia, Pennsylvania 19104.

(1) Lowenstam, H. A.; Weiner, S. *On Biomineralization*; Oxford University Press: Oxford, England, 1989.
(2) Mann, S. *Biomineralization: Principles and Concepts in Bioinorganic Materials Chemistry*; Oxford University Press: Oxford, England, 2001.
(3) Mann, S. *Angew. Chem., Int. Ed.* **2000**, *39*, 3392−3406.
(4) Mann, S. *Nature* **1993**, *365*, 499−505.
(5) Dujardin, E.; Mann, S. *Adv. Mater.* **2002**, *14*, 775−788.
(6) Ozin, G. A. *Acc. Chem. Res.* **1997**, *30*, 17−27.
(7) Weiner, S.; Addadi, L. *J. Mater. Chem.* **1997**, *7*, 689−702.
(8) Estroff, L. A.; Hamilton, A. D. *Chem. Mater.* **2001**, *13*, 3227−3235.
(9) Kato, T.; Sugawara, A.; Hosoda, N. *Adv. Mater.* **2002**, *14*, 869−877.
(10) Cölfen, H.; Mann, S. *Angew. Chem., Int. Ed.* **2003**, *42*, 2350−2365.
(11) Meldrum, F. C. *Int. Mater. Rev.* **2003**, *48*, 187−224.
(12) Yu, S. H.; Cölfen, H. *J. Mater. Chem.* **2004**, *14*, 2124−2147.
(13) Tang, Z. Y.; Kotov, N. A.; Magonov, S.; Ozturk, B. *Nat. Mater.* **2003**, *2*, 413−418.
(14) Gehrke, N.; Nassif, N.; Pinna, N.; Antonietti, M.; Gupta, H. S.; Cölfen, H. *Chem. Mater.* **2005**, *17*, 6514−6516.
(15) Yu, S. H.; Yang, J.; Qian, Y. T. Low Dimensional Nanocrystals. In *Encyclopedia of Nanoscience and Nanotechnology*; Nalwa, H. S., Ed.; American Scientific Publishers: Los Angeles, 2004; Vol. 4, pp 607−647.
(16) Cölfen, H. *Macromol. Rapid Commun.* **2001**, *22*, 219−252.
(17) Yu, S. H.; Cölfen, H.; Antonietti, M. *Adv. Mater.* **2003**, *15*, 133−136.
(18) Qi, L. M.; Cölfen, H.; Antonietti, M.; Li, M.; Hopwood, J. D.; Ashley, A. J.; Mann. S. *Chem.−Eur. J.* **2001**, *7*, 3526−3532.
(19) Qi, L. M.; Cölfen, H.; Antonietti, M. *Angew. Chem., Int. Ed.* **2000**, *39*, 604−607.
(20) Qi, L. M.; Cölfen, H.; Antonietti, M. *Chem. Mater.* **2000**, *12*, 2392−2403.
(21) Yu, S. H.; Cölfen, H.; Antonietti, M. *Chem.−Eur. J.* **2002**, *8*, 2937−2945.
(22) Li, M.; Mann, S.; Cölfen, H. *J. Mater. Chem.* **2004**, *14*, 2269−2276.
(23) Yu, S. H.; Antonietti, M.; Cölfen, H.; Hartmann, J. *Nano Lett.* **2003**, *3*, 379−382.
(24) Li, M.; Schnablegger, H.; Mann, S. *Nature* **1999**, *402*, 393−395.
(25) Li, M.; Mann, S. *Langmuir* **2000**, *16*, 7088−7094.
(26) Muller, T.; Heinig, K. H.; Schmidt, B. *Nucl. Instrum. Methods Phys. Res., Sect. B* **2001**, *175*, 468−473.
(27) Martin, C. R. *Science* **1994**, *266*, 1994.
(28) Hulteen, J. C.; Martin, C. R. *J. Mater. Chem* **1997**, *7*, 1075−1087.

10.1021/la060985j CCC: $33.50
Published on Web 06/30/2006

a solution method with capping reagents,[30] self-assembly of nanoparticles,[31,32] oriented attachment,[33−35] or other methods, and a variety of formation mechanisms were proposed. Only after a full understanding of the formation mechanisms of these materials is complete morphological control possible. In this study, we will reveal the detailed formation mechanisms of $BaSO_4$ fiber superstructures, which are formed by $BaSO_4$ crystallization in the presence of polyacrylate,[18,23] as well as the influence of the substrate on heterogeneous nucleation. This is an example of a deeper mechanistic understanding of a bioinspired crystallization reaction. On the basis of the mechanism, the morphology can be controlled from short cones to longer fiber bundles.

Experimental Section

Materials. The following chemicals were purchased from the indicated suppliers and used without purification: Na_2SO_4 (Aldrich, 99%), $BaCl_2$ (Aldrich, 99%), and polyacrylate sodium salt (PAANa, $M_n = 5100$ g·mol^{-1}) (Fluka). The sodium content of the polymer was reported by the manufacturer to be 19% w/w, implying that only a minority of the carboxyl groups are protonated (∼12.9% molar ratio of carboxylic acid groups; calculation based on elemental analysis).[36] The chemicals for surface modification, including 2-mercaptoethylamine, 2-mercaptoethanol, 2-mercaptoacetic acid, sodium 2-mercapto-1-ethane-sulfonate, sodium 10-mercaptodecanate, 1-dodecanethiol, poly(sodium-4-styrenesulfonate) (PSS, $M_w =$ 70 000 g·mol^{-1}), poly(allylamine-hydrochloride) (PAH, $M_w = 70\,000$ g·mol^{-1}), branched-poly(ethyleneimine) (PEI, $M_w = 25\,000$ g·mol^{-1}) and poly(diallyldimethylammonium chloride) (PDADMAC, $M_w =$ 100 000−200 000 g·mol^{-1}, 20 wt % solution), were purchased from Sigma-Aldrich and used without further purification.

$BaSO_4$ Mineralization. An aqueous solution of 0.6 mL of 0.05 mol·L^{-1} $BaCl_2$ was added dropwise to 15 mL of PAANa (0.56 g·L^{-1}) in a glass bottle under vigorous stirring. After 0.6 mL of 0.05 mol·L^{-1} Na_2SO_4 was added dropwise with continuous stirring for 5 min, the pH was adjusted to 5.6−5.7 using HCl. Then, the solution was transferred into glass or polypropylene bottles and kept standing quiescent for a defined period for mineralization at room temperature (20−22 °C). For all solutions, nondegassed Millipore water was used. Because of the higher solubility of $BaCO_3$ as compared to that of $BaSO_4$, the water did not need to be degassed. The concentrations of the mineral and polymer were chosen on basis of titration experiments of the polymer with Ba^{2+} to keep the free Ba^{2+} concentration and thus supersaturation low in solution.[36] This ensures that the system close to the phase boundary of precipitation but simultaneously contains local regions of high Ba^{2+} concentrations in the polymer aggregates. This is reported in detail in the first part of this series.

Mineralization on Modified Substrates. All of the modified substrates were thoroughly washed with distilled water or ethanol and blown dry with nitrogen prior to use. The mineralization on modified substrates was carried out in a polypropylene bottle. In general, a stock solution was prepared as described above. Then, 1 mL of solution was added to different polypropylene bottles with different modified substrates. Mineralization was performed at room temperature for 3 days. Modified substrates were prepared as follows:

Modification of Substrates by Polyelectrolytes. Silicon wafers (Wacker, Burghausen, Germany; orientation 100, naturally oxidized) were cut and cleaned by the RCA method[37] prior to coating. For the coating, the surfaces were put into a solution of 0.5 mg/mL PEI without added salt for 20 min, rinsed carefully using deionized water (for the PEI coating, the procedure stops here), and immersed into a 1 mg/mL solution of PSS containing 0.5 mol/L NaCl. The samples were washed again (for the PSS coating, the procedure stops here). For the surfaces that were PAH- and PDADMAC-terminated, an additional layer of the respective polymer was adsorbed, using the same conditions mentioned for PSS. The surfaces were stored under water before use.

Modification of Gold Substrates by Thiols with Varying Functional Groups. After thorough washing, the silicon wafer was first coated with 5 nm Cr and then with a 100 nm Au layer using an electron beam evaporator. Thiol solutions were freshly prepared before each adsorption experiment to avoid oxidation in air. The thiol monolayer was formed by exposing Au substrates to aqueous solutions of 2 mmol/L 2-mercaptoethanol, 2-mercaptoacetic acid, sodium 2-mercapto-1-ethane-sulfonate, and sodium 10-mercaptodecanate and an ethanol solution of 2 mmol/L 1-dodecanethiol overnight.

Patterned Gold Surfaces. First, the silicon wafer was covered with a Cu TEM grid without a carbon film as a mask. Then, the wafer was coated with 3.3 nm Cr, followed by a 120.9 nm gold layer using an electron beam evaporator. The TEM grid was removed before mineralization.

Analytical Techniques. *Electron Microscopy.* Scanning electron microscopy (SEM) images were taken with a field emission SEM LEO1550 (Gemini) microscope operating at 3 kV. Samples were prepared by evaporating a drop of water suspension from a glass substrate followed by drying at room temperature.

Transmission electron microscopy (TEM) was preformed on a Zeiss EM 912 Omega microscope. Samples were prepared by evaporating a drop of water suspension of sample from an amorphous carbon-coated Cu TEM grid. Electron diffraction was also performed on a Zeiss EM 912 Omega microscope at 120 kV with a 580 mm camera.

Time-Resolved Optical Microscopy (TROM). Normal optical microscopy images were taken in solution with an Olympus BX41 microscope connected with a MONACOR TVCCD-460 color camera. Time-resolved microscopy (TROM) was measured by phase contrast microscopy as described elsewhere.[38] Briefly, a temperature-controlled (20 °C) observation chamber composed of a glass substrate was filled with solution, tightly sealed, and inspected under a phase-contrast microscope (Zeiss 35, 40, Ph 2). The structures are oriented mainly along the glass substrate but show fluctuation out of the focal plane of the microscope. Suitable defined areas were selected and a TROM video on this selected area was taken over 48 h. Parts of this video can be seen in SI 1. For comparison, a solution in plastic substrates (glass substrates covered with PROLENE X-ray thin film) was also examined close to the substrate.

Dynamic Light Scattering (DLS). The DLS experiments were performed with a laboratory-built goniometer with temperature-controlled (0.05 K) cuvette holders, an attached single-photon detector ALV/SO-SIPD, and a multiple tau digital correlator ALV 5000/FAST from ALV (Langen, Germany). The light source was a PL-3000 He−Ne laser with 34 mW power from Polytec (Germany). Quartz cuvettes (Hellma, Mülheim, Germany) were charged with the freshly prepared stock solutions by directly filtering them through 800 nm pore size filters. Placement of the cuvettes in the tempered holders is defined as $t = 0$. Correlation functions were recorded every 600 s for approximately 16 h.

Results and Discussion

Time-Resolved Observation of Particle Formation and Growth. After the physicochemical characterization of the mineralization process,[36] we applied time-resolved optical microscopy (TROM) to obtain detailed information on the growth and fiber assembly process directly in solution.

(29) Dai, Z. R.; Gole, J. L.; Stout, J. D.; Wang, Z. L. *J. Phys. Chem. B* **2002**, *106*, 1274−1279.
(30) Peng, X. G.; Manna, L.; Yang, W. D.; Wickham, J.; Scher, E.; Kadavanich, A.; Alivisatos, A. P. *Nature* **2000**, *404*, 59−61.
(31) Korgel, B. A.; Fitzmaurice, D. *Adv. Mater.* **1998**, *10*, 661−665.
(32) Wyrwa, D.; Beyer, N.; Schmid, G. *Nano Lett.* **2002**, *2*, 419−421.
(33) Penn R. L.; Banfield, J. F. *Geochim. Cosmochim. Acta* **1999**, *63*, 1549−1557.
(34) Tang, Z. Y.; Kotov, N. A.; Giersig, M. *Science* **2002**, *297*, 237−240.
(35) Polleux, J.; Pinna, N.; Antonietti, M.; Niederberger, M. *Adv. Mater.* **2004**, *16*, 436−439.
(36) Wang, T.; Cölfen, H. *Langmuir* **2006**, *22*, 8975−8985.
(37) Kern, W.; Puotinen, D. A. *RCA Rev.* **1970**, *31*, 187−206.
(38) Reinecke A.; Döbereiner, H. G. *Langmuir* **2003**, *19*, 605−608.

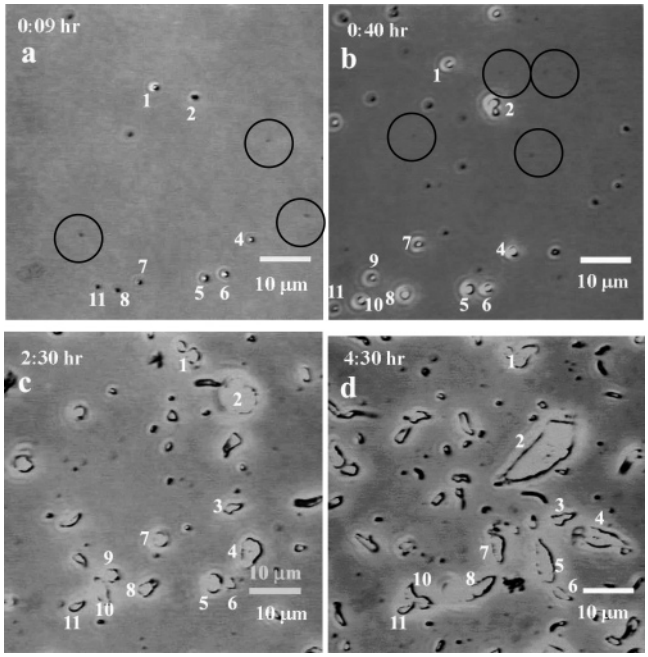

Figure 1. Selected images of time-dependent optical microscopy from a constant area at different crystallization times: (a) 9, (b) 40, (c) 150, and (d) 270 min. The sample was examined in solution at a constant temperature of 20 °C. (See SI 1 for the video and PowerPoint file with a full snapshot sequence of the whole mineralization process up to 24 h.) Note that the motionless particles in the images are numbered with fixed numbers throughout a−d. They might change their positions slightly as a result of convection and growth. Several fast-moving particles in images a and b are marked by circles.

TROM shows that there is no obvious aggregation of microscopic species in the glass sample cell after the addition of $BaCl_2$ to the PAANa solution. This is probably a result of the short chain length of PAANa and the resulting small aggregate size[39] because it is well known that polyacrylates are cross linked by Ca^{2+}, leading to their precipitation.[40] Therefore, as a result of their interaction with bivalent cations combined with good dispersing effects, polyacrylates are used as water dehardeners.[41,42] This should be similar for Ba^{2+} because it is also a bivalent ion binding to polyacrylate.[36] Indeed, Ba^{2+}−PAANa complexes could be detected by analytical ultracentrifugation in the first part of this series[36] but not DLS, probably because their size and concentration are too small.

After Na_2SO_4 was added, a few motionless nanoparticles of micrometer size were observed (Figures 1 and SI 1). These aggregates are mainly amorphous $BaSO_4$ nanoparticles but with partially crystalline characteristics, as revealed by TEM and selected-area electron diffraction (Figure SI 2a). They are precursors to the crystalline fiber bundles (Figure SI 2b). Similar amorphous precursors (e.g., amorphous $CaCO_3$) were also found in other mineralization systems.[43−45] This finding agrees with our earlier report that the precursor species of the $BaSO_4$ fiber bundles is an aggregate of amorphous precursor particles.[18] Besides these aggregates, there are several smaller nanoparticles with fast Brownian movement. Because of the light-scattering effect, these nanoparticles are visible in TROM, although their sizes are below the resolution of the optical microscope. Their sizes cannot be determined exactly from TROM images only. However, their sizes can be estimated to be around 400 nm by comparison with the moving speed of monodisperse latex particles of known size, whereas the smaller nanoparticles cannot be excluded because they cannot be monitored, which is due to their movement being too fast. The amorphous primary particles in Figure SI 2a are smaller with a size of about 60−100 nm, indicating that the moving particles in Figure 1a are aggregates of nanoparticles. This is in agreement with a time-dependent DLS study that shows particles with 80−120 nm diameters at times up to 16 h, indicating that the primary nucleated species must be nanoparticles of this size (Figure SI 3, which displays radii). Because the larger species (>400 nm) are not seen in DLS, it can be assumed that they stick to the quartz surface of the light-scattering cuvettes, whereas the small nanoparticles are present in solution and can be detected.

With increasing time (Figure 1b), more particles nucleate. Similar to Figure 1a, most of them are moving at a comparable speed with respect to the 400 nm particles. Even up to 15 h, new moving particles of about 400 nm size are generated, which indicates continuous particle nucleation and aggregation as long as the supersaturation has not dropped to 1 at 15 h.[36] The supersaturation is defined as $S = \{[SO_4^{2-}][Ba^{2+}]/K_{sp}\}^{0.5}$, where $[SO_4^{2-}]$, $[Ba^{2+}]$, and K_{sp} are the concentrations of free SO_4^{2-} ions and free Ba^{2+} ions and the solubility product of $BaSO_4$, respectively. The time-dependent supersaturation was obtained from a series of calculations based on time-dependent pH measurement, which are shown in detail in ref 36. This is seemingly contradictory to the heterogeneous nucleation mechanism for the system identified in ref 18. However, the result from a control TROM experiment in a plastic sample cell indicates that the substrate plays an important role in the nucleation process, and this is in accordance with our earlier findings about heterogeneous nucleation on glass surfaces.[18] When the solution is kept standing quiescent on a plastic substrate (Prolene X-ray thin film) for up to 24 h, no particles are found during the entire observation period in the light microscope, underlining the importance of polar glass surfaces for the nucleation of $BaSO_4$ fiber structures. Consequently, the moving particles in solution, which are visible in the optical microscope, can only be those heterogeneously nucleated and subsequently detached from the substrate. In addition, amorphous precursor particles must also be present in the late experimental stages, even if the supersaturation approaches 1.

With continuous nucleation and the generation of more moving aggregates in solution after 40 min, the aggregates slowly become larger and finally motionless because of their size and reattachment to the substrate. Subsequently, some of the larger fixed aggregates generate fibrous conelike structures. After 150 min (Figure 1c), the first fixed fibrous assemblies (see also the SEM micrographs in Figure 2) become visible, although many larger fixed micrometer-sized spherical particles are also observed. After 270 min (Figure 1d), most of these spherical particles became fixed fibrous particles besides the small moving nanoparticles that are continuously generated. This suggests that the fixed spherical particles act as a material depot for the formation of the fibrous structures or that they are developing fiber cones viewed from the top. It is interesting that particles 2, 4, and 5 in Figure 1c and d appear to be attached to the glass surface at

(39) Molnar, F.; Rieger, J. *Langmuir* **2005**, *21*, 786−789.
(40) Volk, N.; Vollmer, D.; Schmidt, M.; Oppermann, W.; Huber, K. *Adv. Polym. Sci.* **2004**, *166*, 29−65.
(41) Rieger, J.; Hadicke, E.; Rau, I. U.; Boeckh, D. *Tenside, Surfactants, Deterg.* **1997**, *34*, 430−435.
(42) Rieger, J. *Tenside, Surfactants, Deterg.* **2002**, *39*, 221−225.
(43) Faatz, M.; Cheng, W.; Wegner, G.; Fytas, G.; Penciu, R. S.; Economou, E. N. *Langmuir* **2005**, *21*, 6666−6668.
(44) Faatz, M.; Gröhn, F.; Wegner, G. *Adv. Mater.* **2004**, *16*, 996−1000.
(45) Rieger, J.; Thieme, J.; Schmidt, C. *Langmuir* **2000**, *16*, 8300−8305.

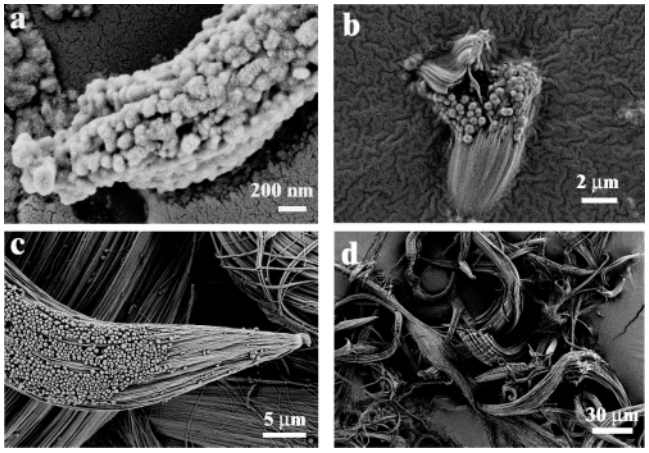

Figure 2. Typical SEM images at different mineralization times: (a) 15 min, (b) 6 h, (c) 12 h, and (d) 18 h. Samples were prepared by evaporating a drop of water suspension from a glass substrate and then drying at room temperature.

their wide side (see also video SI 1) before they detach from the surface, showing their conelike structure when viewed from the side.

An SEM measurement of the dried sample provides closer observation and further evidence for the nanoparticles in solution (Figure 2a), although the artifact from the preparation of SEM samples is difficult to rule out. In the early stages, nanoparticles with sizes of about 100−200 nm were observed. These particles are heavily aggregated, possibly upon sample preparation, because they were not observed in solution. The smaller size, as compared to the ca. 400 nm in solution by TROM, could also be indicative of a highly hydrated amorphous precursor particle in solution, which loses its water upon SEM sample preparation.

Then, at about 6 h, nanoparticles around 400−500 nm and small fibrous aggregates of micrometer size were observed (Figure 2b). Although most of the structures are very long fibers at longer mineralization time (e.g., 12 h) (Figure 2c), spherical nanoparticles (250−500 nm) with sizes corresponding to the above-discussed primary amorphous particle aggregates can also be seen. The spherical nanoparticles vanished after about 18 h (Figure 2d), and a variety of different fiber architectures were found, indicating the unstable amorphous character of the spherical aggregates and their transition to crystalline fibers.

Substrate Effects and Patterned Crystallization. Our earlier report[18] and control experiments from TROM in glass and plastic vessels show that heterogeneous nucleation on glass surfaces plays an important role. Crystallization on a silicon wafer modified with different polyelectrolytes or gold surfaces modified with different functional groups prove that the substrate has a large influence on the generation of $BaSO_4$ fibers. Hydrophilic substrates modified with hydroxyl, carboxyl, sulfonate, or amino functionalities led to fibrous structures, whereas the hydrophobic surfaces, for example, Au, plastic, or Au modified with 1-dodecanethiol, did not induce particle formation. Interestingly, the fibrous morphologies obtained from different substrates (sulfonate-, carboxylate-, or amino functionalized) are different from each other (Figure SI 4 and 5). The possible reason might be different charges or a cooperative effect from different functionalities on the substrate and PAANa molecules, but the exact mechanism is still not clear. However, these results indicate that the $BaSO_4$ fibers can grow only on polar hydrophilic surfaces with hydroxyl, carboxyl, and amine functionalities instead of hydrophobic ones such as alkyl-terminated monolayers, gold surfaces, or plastic substrates (see images in Figure SI 4 and SI 5). This can be nicely proven by a TEM-grid-patterned silicon

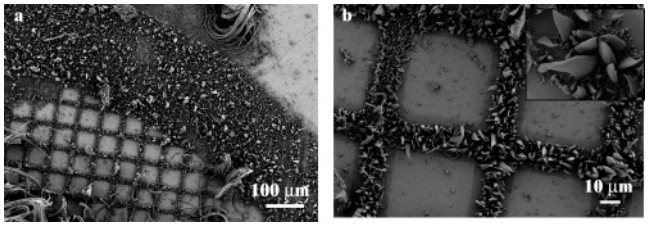

Figure 3. SEM micrograph of (a) a $BaSO_4$ fiber pattern grown on a silica wafer partially covered by gold with a TEM Cu grid pattern taken out of the crystallization solution after 1 day and (b) enlargement of image a. Fibers grew only on the silica wafer substrate without gold (dark area and lines). No fibers were formed on the gold surface (bright square area), and the few particles found in this area could be detached particles, which were deposited in these areas by the drying process.

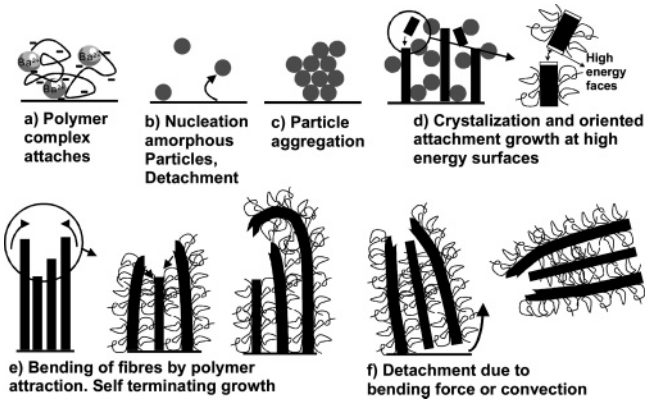

Figure 4. Schematic presentation of the growth of $BaSO_4$ fiber bundles from an initially surface attached Ba^{2+}−PAA complex at high supersaturation $S > 2$.

wafer, where the noncovered waver regions with the shape of the quadratic holes of the TEM grid were coated with a gold film. Applying this silicon wafer as a template for $BaSO_4$ fiber nucleation in a plastic bottle led to a pattern of the nucleated fibers clearly following the grid lines, which mark the polar silicon surface (Figure 3), whereas on the gold-coated square areas no particles are nucleated. In addition, a closer look at higher resolution (Figure 3b inset) reveals that the wide fiber bundle edge is always attached to the surface and that the fiber bundle gets thinner with progressing fiber growth. This is in accordance with the TROM result (Figure 2c and d) and the mechanism of fiber bundle formation at high $BaSO_4$ supersaturation discussed below (Figure 4).

Mechanisms for $BaSO_4$ Fiber Superstructure Generation. Solution methods including AUC, pH, and conductivity measurements imply that PAA−Ba^{2+} complexes and aggregates are the first formed species in the formation process of $BaSO_4$ fibers.[36] In addition, it has already been revealed that most of the Ba^{2+} ions are complexed by PAA. Thus, the complex acted as the first formed species in the complicated mineralization mechanism, which releases Ba^{2+} slowly because of the competition of $RCOO^-$ with the SO_4^{2-} ions.[36] The formation of a PAA/Ba^{2+} complex is also the reason that the supersaturation is so low compared to that of normal crystallization reactions. Therefore, the higher supersaturation that we state in this study is relative only to the lower and vanishing supersaturation in later experimental stages. Time-resolved microscopy methods (SEM, TEM, and TROM) and DLS show that amorphous nanoparticles of 60−100 nm diameter are the primarily nucleated species that form aggregates as precursors to $BaSO_4$ fibers. Nevertheless, there are three different pathways for the formation of the fiber superstructures depending on the supersaturation. Another factor is the number

of available nanoparticles for the formation of the fiber bundles. Reproducible measurements of the time-dependent supersaturation show that the supersaturation in the first 220 min, which is the relevant time frame for the particles shown in Figure 1, exceeds $S = 2$.[36] However, although the supersaturation allows us to distinguish the three superstructure formation pathways, the values of supersaturation are chosen somewhat arbitrarily. This is because there is no sharp transition between the formation pathways of different structures and three different fiber superstructures remain in the final stage.

1. High Supersaturation (S > 2): Fiber Bundles with Flat Growth Edges. On the basis of the above presented results, a four-step process involved in fiber bundle formation can be formulated: (a) primary particle nucleation (Figure 4a and b), (b) attachment/detachment from the substrate (Figure 4b and c), (c) further growth of the substrate-immobilized particles and fiber bundle formation (Figure 4d), and (d) structure optimization (Figure 4e).

a. Heterogeneous Nucleation of Primary Particles (Figure 4a and b). The first formed species in the early solution are Ba^{2+}–polyacrylate complexes,[36] resulting in a highly localized Ba^{2+} concentration. Without polymer, for the given Ba^{2+} concentration, the supersaturation would be much higher with $S = 179$, as calculated for comparable conditions in the first article of this series.[36] The experimentally determined total Ba^{2+} concentration released from the polymer complexes is about 20−100 higher than the free Ba^{2+} concentration in solution, depending on the reaction time.[36] This means that the complexes are the centers with high supersaturation. This is in contrast to the usual situation without polymers, where amorphous particles are nucleated in solution at high supersaturation.

However, these complexes must be on the nanometer scale[39] because they are not visible in optical microscopy, not even by their light-scattering effect like the aggregates in Figure 1a, and they could not be revealed by a control experiment after Ba^{2+} addition to a polyacrylate solution. However, they can be detected by analytical ultracentrifugation.[36] Control experiments on substrates of different polarity show that the primary nucleated particles are formed by heterogeneous nucleation. This implies that the complexes attach to the surface of glass or other hydrophilic substrates, resulting in a high local Ba^{2+} concentration (Figure 4 a) and acting as nucleation centers for $BaSO_4$. Because $BaSO_4$ ($K_{sp} = 1.07 \times 10^{-10}$ mol^2/L^2) is less soluble than $BaCO_3$ ($K_{sp} = 2.58 \times 10^{-9}$ mol^2/L^2),[46] the competition of sulfate ions with the polymer carboxylate groups should result in the release of Ba^{2+} from the polymer to form $BaSO_4$, but with the polymer still attached to the formed particle. This can explain why the primary formation of amorphous nanoparticles (Figure 4b) at the high local polymer concentration can inhibit crystallization.

b. Attachment/Detachment on the Substrate (Figure 4b and c). The formed primary particles are amorphous structures of 60−100 nm size (Figure SI 2 and DLS Figure SI 3) and may either detach from the surface or stay on the substrate (Figure 4b). However, because of the high supersaturation in the initial experimental stages, homogeneous nucleation in solution is also possible. The aggregates of amorphous nanoparticles will grow. Because of the high local Ba^{2+} concentration in the polymer complexes along the glass surface, the immobilized particles can grow more quickly and the moving particles will grow more slowly as a result of the lower local Ba^{2+} concentrations (Figure 4c). With increasing time, more moving free particles become available, as shown in the video in SI 1.

c. Aggregation, Crystallization, and Fiber Growth by Oriented Attachment (Figure 4c and d). The above results clearly show the existence of amorphous particles: ca. 400 nm particles estimated by OM, 100−200 nm precursor particles shown in Figure 2, 60−100 nm amorphous primary particles in the aggregates shown in Figure SI 2, and 60−120 nm particles at up to 16 h from DLS, respectively (Figure SI 3). These observations are in agreement with our previously published results for amorphous precursors.[18] However, the time-dependent DLS study also reveals that the particle diameter stays constant at 60−80 nm diameter after 1 h up to the observation limit of 16 h. This gives evidence that primary particles or small aggregates are present at all stages of the experiment, although their concentrations are decreasing with time as a result of transformation into aggregates and finally fiber bundles. The larger particles with sizes up to 120 nm observed by DLS within the first hour of the experiment vanish, likely because of attachment to the surface or surface-attached aggregates that are already present.

The particles attached to the substrate serve as aggregation centers for additional particles from solution (Figure 4c). This is in contrast to fibrous calcite, which has been reported to form by a solution−precursor−solid mechanism.[47] In our case, the amorphous particles can serve as crystallization precursors and then transform into crystalline particles.[48,49] However, when crystallization starts, the polymer can coat the crystal surfaces, transforming them into high-energy (no adsorbed polymer) and low-energy (adsorbed polymer) surfaces.[50] It has been repeatedly reported that such particles can significantly reduce their surface energy by means of the oriented attachment mechanism, where equal high-energy surfaces of two nanoparticles crystallographically combine and fuse to form a single crystal.[33−35] This mechanism is not only limited to transition-metal oxide systems but also was found for classical minerals such as $CaCO_3$.[51] In the case of $BaSO_4$ fiber formation, oriented attachment along the high-energy (210) face, which is not covered by polymer, leads to the formation of single-crystalline $BaSO_4$ fibers by further attachment of surface-coded crystalline building units. Indeed, from HRTEM data, [210] was identified as the fiber axis (Figure SI 6). Oriented attachment can be deduced for the formation of the single-crystalline $BaSO_4$ fibers for the following reasons: (a) Single-crystalline fibers are formed without defects or branches. If the crystal growth is solely controlled by selective polymer adsorption, then the structures are never perfectly homogeneous, but branching occurs as a result of inhomogeneities in polymer adsorption.[52] (b) The fiber growth process is particle-based according to the time dependence of supersaturation:[36] $S \approx 1$ constantly after 15 h. Nevertheless, a development of the fibers can still be observed, although it cannot occur via dissolution−recrystallization anymore because of the vanishing driving force for crystallization. (c) The (210) face perpendicular to the [210] fiber axis always exposes negative sulfate ions. This hinders polyacrylate adsorption due to electrostatic repulsion

(46) Lide, D. R., Ed. *CRC Handbook of Chemistry and Physics*, 73 ed.; CRC Press: Boca Raton, FL, 1992−1993; pp 8−43.

(47) Olszta, M. J.; Gajjeraman, S.; Kaufman, M.; Gower, L. B. *Chem. Mater.* **2004**, *16*, 2355−2362.

(48) Politi, Y.; Arad, T.; Klein, E.; Weiner, S.; Addadi, L. *Science* **2004**, *306*, 1161−1164.

(49) Aizenberg, J.; Muller, D. A.; Grazul, J. L.; Hamann, D. R. *Science* **2003**, *299*, 1205−1208.

(50) Addadi, L.; Weiner, S. *Proc. Natl. Acad. Sci. U.S.A.* **1985**, *82*, 4110−4113.

(51) Gehrke, N.; Cölfen H.; Pinna, N.; Antonietti, M.; Nassif, N. *Cryst. Growth Des.* **2005**, *5*, 1317−1319.

(52) Antonietti, M.; Breulmann, M.; Göltner, C. G.; Cölfen, H.; Wong, K. K. W.; Walsh, D.; Mann, S. *Chem.−Eur. J.* **1998**, *4*, 2493−2500.

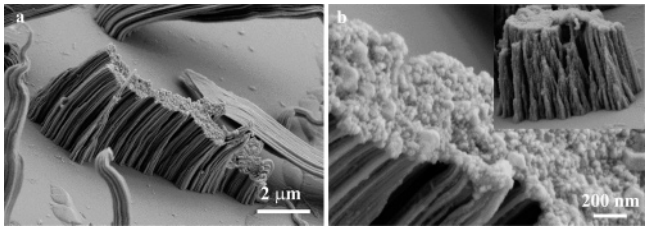

Figure 5. (a) Growth edge and (b) high magnification of the growth edge of a $BaSO_4$ fiber bundle after 20 min. The magnified view of a fiber construction site on the surface (inset) shows that several fiber sub-bundles are formed, which terminate in a single tip.

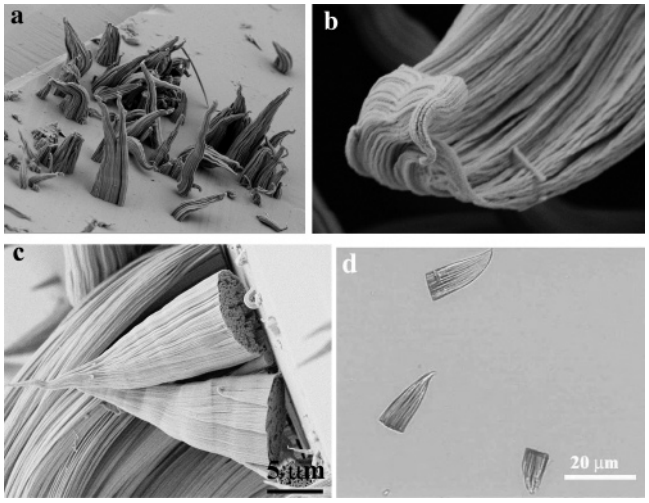

Figure 6. SEM micrograph of (a) a $BaSO_4$ fiber pattern grown on a glass surface in the presence of polyacrylate after 1 h; (b) typical magnified view of the sharp tip exhibiting a bending end; (c) fibers detaching from the substrate, where their porous inner structure is clearly visible; and (d) optical microscopy from solution after 2 h.

and makes this face a high-energy surface. Such a face is well suited for crystallographic fusion according to the oriented attachment mechanism.[12] (d) The structure of the $BaSO_4$ unit cell and the special anion-terminated (210) surface structure (displayed as red lines in Figure 15 in ref 12) allow for the crystallographic fusion of two (210) faces although their surfaces predominantly expose sulfate ions.

Further evidence for the particle-based mechanism of the fiber bundle growth can be obtained from a high-magnification image of the edge of a growing fiber bundle. These structures clearly show associated particles with a typical size of 25−50 nm, partly forming larger aggregates (Figure 5a and b). These particles form the rough growth surface (Figure 4d), whereas the side faces of the fiber bundle are relatively smooth, indicating their crystallized character. This situation corresponds to the scheme in Figure 4d, giving further evidence for the oriented attachment mechanism.

d. Structure Optimization, Fiber Bundle Formation, and Particle Detachment (Figure 4e and f). The primary structures in Figure 5a continue their growth into defined fiber structures by a further self-optimization process. The simultaneous growth of several fibers from a glass surface is shown in Figure 6a, in agreement with the sketch in Figure 4e, and clearly reveals that in this case the fiber growth does not start from a single tip[18] but rather from the simultaneous nucleation and growth of several neighboring fibers from a surface-attached aggregate of amorphous particles. The common fiber lengths in a forming bundle are still relatively equal, whereas the growth surface is rough because of the particle attachment from the solution phase (Figure 5). Because neighboring fibers in a bundle do not all have the same length during their growth process, fibers that extend the fiber majority can attract each other by van der Waals attraction. This interaction is generally present at the long axes of the fibers in close proximity. In addition, electrostatic interaction between polyacrylate and several $BaSO_4$ fibers in close proximity can take place with the effect of fiber cross linking via the attachment of polyacrylate polymer to two fibers. Both effects lead to fiber bending and self-terminating growth (Figure 4e), which is in agreement with the mechanism suggested for the self-termination of $BaSO_4$ fibers formed in a reverse microemulsion.[25] Figure 6b shows the bending of a fiber bundle tip as a result of these interactions. The bending directions during the proceeding growth of a fiber bundle can also vary as shown in Figure SI 7. The distance between the fibers appears to increase from the tip to the broad end, also indicating the created internal stress due to bending.

The fiber bundles are attached to the glass or wafer surface very loosely because a majority of the fibers detach, possibly resulting from internal stress due to fiber bending, convection in the mineralization solution, or sample preparation for microscopy investigation (Figures 4f, 6c and d, and the video in SI 1). The detachment of the fibers also reveals their inner structure (Figure 6c). The fiber bundles are by no means solid bodies, as are their densely packed bundle analogues found in the presence of double hydrophilic block copolymers (DHBCs),[18,21] but are porous.[23] This can be attributed to the more limited particle stabilization capability of polyacrylate as compared to a DHBC with a polyacrylate or similar sticking block.[16] Therefore, empty spaces are generated in the forming fiber bundle, indicative of insufficient particle building material.[36] In addition, the empty spaces in a bundle of single-crystalline fibers are further evidence of the particle-based growth mechanism by oriented attachment.

A control experiment applying a different addition sequence of SO_4^{2-} and Ba^{2+} to the PAANa solution provides more evidence for the importance of the Ba−PAANa complex in the formation of $BaSO_4$ fiber bundles. If Na_2SO_4 is first added to a PAANa solution, then no complex is formed because sulfate does not combine with the carboxylate groups of PAANa. When $BaCl_2$ is added to the mixture, most Ba^{2+} ions directly combine with SO_4^{2-} because of the low solubility product of $BaSO_4$. This generates more nanoparticle precursors as compared to the case where $BaCl_2$ is added first. Consequently, more fibers with smaller sizes were obtained in this case (Figure SI 8).

2. Low Supersaturation ($S = 1.05-2$): Nucleation of Fiber Bundles from a Single Nucleation Spot. With the decrease in supersaturation from $S = 2$ at 230 min to $S = 1.02$ at 900 min and proceeding fiber growth,[36] a second competing growth mechanism can be observed (Figure 7). Here, amorphous particles are nucleated either at the glass surface or homogeneously in solution (Figure 7a). If particles attach to the surface, then they form aggregates (Figure 7b) in agreement with the first mechanism (Figure 4c), but the difference is that these aggregates are much smaller because of the lack of sufficient primary particles. However, the crystallization step and the subsequent oriented attachment to form the fiber bundles (Figure 7c) are the same as in the first mechanism (Figure 4d).

The important difference from the first mechanism, however, is insufficient building material. Only single nucleation spots are formed at the glass surface, resulting in an initial single fiber formed by heterogeneous nucleation (Figure 7c) instead of an array of nucleation spots in the first mechanism (Figure 4). As amorphous particles attach to existing fibers (Figure 2), additional fibers nucleate around an existing fiber (Figure 7d). Here the attraction between the polymer and the fibers, combined with

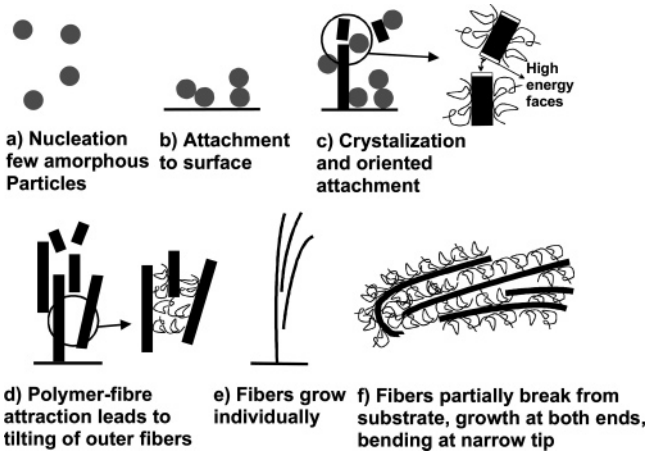

Figure 7. Schematic presentation of the growth of $BaSO_4$ fiber bundles in later experiment stages and the coupled low supersaturation ($S = 1.02-2$) compared to that in Figure 4.

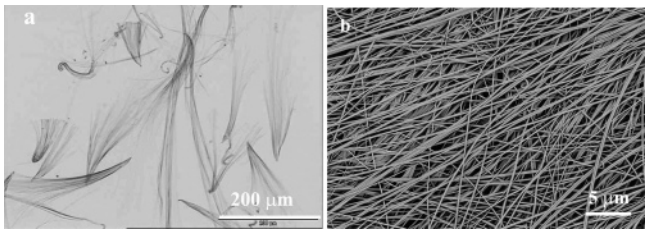

Figure 8. (a) Light microscopy image taken after 1 day and (b) SEM images of $BaSO_4$ fibers observed in addition to a minor part of other morphologies after 2 weeks.

imperfect packing, leads to a tilting out of the outer fibers. Then, the fibers grow individually by oriented attachment, leading to the loose fiber bundles with a nonuniform growth edge as shown in Figures 7e and 8. This is in contrast to the fibers with a flat growth edge formed according to the first mechanism (Figure 4). Upon drying, the individual fibers, which are separated in solution (Figure 8a), attract each other and thus lead to fiber aggregates with uniform thickness and lengths of hundreds of micrometers as observed by SEM (Figure 8b).

It has to be noted that curved and curled tips can be observed for several fiber bundles. This can occur after a fiber bundle has detached from its nucleation surface by convection and both ends of the fiber can grow. Because the fibers attract each other via the polymer and van der Waals attraction as discussed above for the first mechanism, fiber bending can be observed. This leads to bending and curling of the sharp fiber tip and even to self-terminating growth as shown schematically in Figure 7f and as also evident in Figure 8a.

Figure 9 shows a typical growth sequence for a fiber formed from a single nucleation spot. It is clear that the fiber is growing from the sharp tip to the wide end (Figure 9a−d), finally resulting in a long brushlike end at about 150 min (Figure 9e) that grows further until 330 min (Figure 9f). It is notable that this growth sequence begins quite early (<70 min), when the supersaturation is still high ($S = 2.47$). Here, the majority of particles should nucleate according to the first mechanism for high supersaturation. However, there is always the probability that nucleation occurs in a very small aggregate of amorphous particles. Thus, fiber formation from a single nucleation spot can happen at high supersaturation, which tends to produce large surface-attached aggregates of the primary amorphous particles.

3. Vanishing Supersaturation (S = 1.00−1.05): Nucleation of Fiber Bundles with Repetitive Growth Patterns from a Single Nucleation Spot. In the final experimental stages, where the supersaturation approaches $S = 1$, a third growth mechanism begins. It leads to the most complex fiber aggregate structures of the three mechanisms observed in this study. The initial stages (Figure 10a−d) are the same as for the second mechanism, schematically shown in Figure 7a−d. However, the amount of available amorphous building material is less than that in the earlier experimental stages, when the fiber bundles are formed according to the first two mechanisms. Consequently, an approaching amorphous or crystallized building block has the time to choose between several sites for oriented attachment. This enables the choice of optimum attachment sites. Such sites are holes in the growth edge, where an existing fiber is surrounded by longer fibers. Here, the attaching building block is attracted from all sides, except at the surface of the growing edge. This favors the attachment of particles in holes in the fiber bundle growing edge, rather than on the growing edge, so that a "self-healing" surface with a flat growth edge is generated (Figure 10e).

In addition, a dipole moment of the growing fiber comes into play, which is linearly proportional to the fiber length. This has already been considered to explain the nucleation of fiber cones on the rim of an existing fiber cone for the system of $BaCrO_4$ with a DHBC additive.[21] The explanation of why a dipole moment can be generated by heterogeneous nucleation is as follows.

A $BaSO_4$ crystal has a mirror plane perpendicular to the *c* axis. Consequently, if $BaSO_4$ is homogeneously nucleated in solution, then opposite crystal faces are identical in surface structure and composition. This situation is different if the fiber is heterogeneously nucleated on a charged surface. If we take a negatively charged glass surface, then the first crystal layer will be cationic or at least will be enriched in cations. This end of the fiber is determined by the heterogeneous surface, and the other, by the solution interface. In our particular example, the solution is enriched in SO_4^{2-} compared to Ba^{2+}, which is partially complexed by polyacrylate.[36] Thus, the solution end of the growing fiber will be sulfate-terminated or enriched in sulfate. Therefore, both ends of the fiber have different charges, in contrast to a fiber formed by homogeneous nucleation in solution. A fiber with two oppositely charged ends generates a dipole with a dipole moment that is linearly proportional to the distance between the charges on the opposite ends of the fibers. In other words, the dipole moment is proportional to the fiber length, and the growth of the fiber consumes energy to increase the dipole moment.

However, it was mentioned above that the number of nanoparticle building units is low in this crystallization regime. Because homogeneous and heterogeneous nucleation always compete with the particle-mediated oriented attachment mechanism, their importance as a crystal growth pathway increases with decreasing nanoparticle building unit concentration. Therefore, crystal growth becomes selective between particle and ion-mediated growth, with the latter taking the form of heterogeneous nucleation. If an approaching nanoparticle has the choice between a short fiber, just starting to grow after heterogeneous nucleation, and a longer fiber, with a considerable dipole moment, then the particle will attach to the shorter fiber to minimize the energy of the system. Homogeneous nucleation is unimportant here because of the low supersaturation.

Therefore, the dipole moment of the growing fiber increases until a critical value is reached, where the heterogeneous nucleation of a new fiber bundle on the uniform growth edge of the parental bundle becomes energetically more favorable than the further growth of the parental bundle and thus the increase in the dipole moment. This leads to self-limiting growth and the formation of several fiber generations grown on the parental

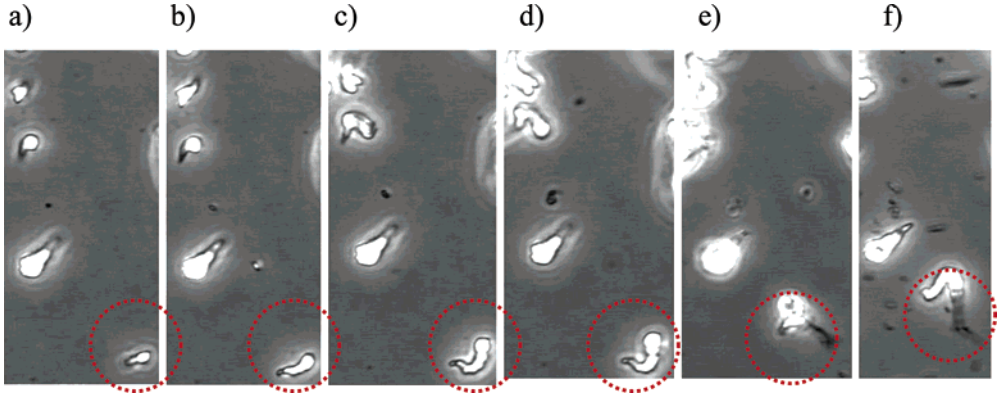

Figure 9. Series of TROM images from the same observed area at different crystallization times for the competitive mechanism of a fiber bundle growing from a single nucleation spot: (a) 70, (b) 80, (c) 95, (d) 120, (e) 150, and (f) 330 min. The sample was examined in solution at a constant temperature of 20 °C.

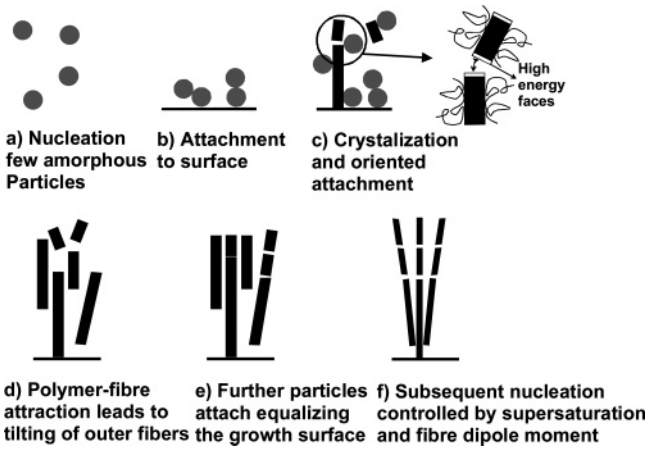

Figure 10. Schematic presentation of the growth of $BaSO_4$ fiber bundles in the final experimental stages and the supersaturation approaching $S = 1$.

Figure 11. (a) Light microscopy and (b, c) SEM pictures of $BaSO_4$ fiber bundles formed in the presence of polyacrylate in the final experimental stages. Note the repetitive growth patterns.

ones as shown schematically in Figure 10f and as the typical growth rings/striations in Figure 11. Typically, in this situation, the fiber bundles show a region of longer fibers that were formed at higher concentrations of nanoparticle building units and then the typical growth striations indicative of the self-limiting growth process.

The length of the fibers is not always uniform until a new bundle is generated (Figure 11a). This illustrates the counterplay between (a) supersaturation defining the driving force for heterogeneous nucleation, (b) the increasing dipole moment, which limits the fiber growth, and most importantly (c) the available building material for oriented attachment, which is coupled to fiber growth according to the first two mechanisms outlined in Figures 4 and 7.

The amount of available building material can also explain the apparent contradiction of why only in the final experimental stages the dipole moments play a role in self-limiting growth and why the fibers do not always have the same length until another generation is nucleated. As long as sufficient building material is available, the ion-mediated heterogeneous particle nucleation virtually does not occur, and selectivity between the particle and ion-mediated crystallization pathways is not yet possible. Therefore, the fibers can grow hundreds of micrometers long without a growth limitation in the early experimental stages. Only for a very small amount of particulate building material in the final experimental stage does the particle growth becomes selective, and heterogeneous nucleation gains importance and dipole moments coupled with heterogeneous nucleation can trigger the self-limiting growth of complex fiber bundle structures. This means that fiber bundle structures, which are formed according to the first two mechanisms outlined in Figures 4 and 7, can serve as heterogeneous nucleation surfaces for the self-limiting growth of further fiber bundle generations, when the amount of particulate building material gets low.

Conclusions

We have shown that the crystallization mechanism of the polymer-controlled $BaSO_4/BaCrO_4$ crystallization into complex fiber bundle structures in aqueous systems, already reported in the literature, is far more complex than previously assumed.[18−23] Three different competing mechanisms were revealed for the polyacrylate-controlled growth of $BaSO_4$ fiber bundles. These mechanisms are in agreement with all earlier published findings and can explain the variety of different fiber bundle structures observed in our study and also in previous reports.[18−23] Oriented attachment[33−35] could be deduced to be responsible for the defect-free formation of single-crystalline fibers. Consequently, the amount of particulate building material is of great importance to the crystallization mechanism.

(a) In the early experimental stages with a large number of nanoparticle precursors and surface-attached Ba^{2+}−polyacrylate complexes, nucleation arrays are formed, where the fiber bundles are nucleated at their broad end and become narrower with growth as a result of attraction between the fibers or because of increasing depletion of building material (mechanism 1, Figure 4). As a characteristic, fiber bundles formed according to this mechanism always have a flat, uniform wide edge and are rather closely packed.

(b) If the supersaturation is lowered, then few aggregates and only single nucleation spots are formed. The fibers are nucleated in the opposite way, namely, with a single fiber tip, and become broader with time upon additional fiber attachment (mechanism 2, Figure 7). Typical fibers formed via this mechanism are nonuniform and exhibit wide ends and loose fiber packing that is especially visible at the wide fiber end.

(c) The third mechanism (Figure 10) can be observed in the final experimental stages with the characteristic depletion of

Figure 12. Snapshot from polyacrylate-controlled $BaSO_4$ crystallization in the final stage of the mineralization experiment. The numbers indicate particles formed according to mechanisms 1−3 outlined in Figures 4, 7, and 10.

particulate building material and thus the oriented attachment mechanism. Here, a counterplay between secondary nucleation and dipole moments leads to self-limiting growth, where secondary nucleation takes place as soon as the dipole moment of a fiber reaches a critical value. Striations and repetitive growth are typical of fibers formed according to this mechanism.

These three mechanisms compete, and the typical structures formed by these crystallization pathways can be found simultaneously in the late experimental stages (Figure 12).

This fact leads to complicated experimental conditions that will exclusively lead to one of the three fibrous superstructures. Only in the very early experimental stages can a predominant reaction according to the first mechanism for high supersaturation be expected. In the later stages, only mixtures of particles formed via different mechanisms are obtained. Different crystallization pathways appear to be simultaneously used depending on the locally available number of precursor nanoparticles.

In addition to the crystallization mechanisms, we were able to show that hydrophilic substrates are needed for the heterogeneous nucleation of the first crystalline species in the fiber bundle structure. Even patterning of the fiber bundle growth could be achieved, which shows the control over such crystallization processes once the formation mechanisms are understood. It is obvious that the surface charge has an influence on the morphology, but the detailed effect still needs to be investigated further.

The above crystallization scenario shows how complicated it can be to reveal crystallization mechanisms in biomimetic mineralization reactions. This will be even more severe in the usual biomineralization processes, where several competing but different crystallization pathways can be found. Time-resolved investigations are very useful in revealing such mechanisms, and it is hoped that more can be learned about other complex additive-controlled crystallization events in similar studies.

Acknowledgment. The Max-Planck Society is gratefully acknowledged for financial support and a fellowship for T.W. We acknowledge Dr. Andreas Erbe for the time-resolved DLS measurements, Margit Barth and Denis Gebauer for help with fiber sample preparation, Rona Pitschke and Dr. Jürgen Hartmann for TEM and electron diffraction measurements, and Dr. An Wu Xu for evaluation of the fiber growth axis. We also thank Marc Nolte and Annelies Heilig for the supply of modified crystallization substrates.

Supporting Information Available: SEM, TEM, electron diffraction, and DLS data and a video of the growing particles. This material is available free of charge via the Internet at http://pubs.acs.org.

Note Added after ASAP Publication. This article was released ASAP on June 30, 2006. Parts a and b were added to Figure 6, and the correct version was posted on August 17, 2006.

LA060985J